Med Biol Eng Comput (2016) 54:411–419
DOI 10.1007/s11517-015-1325-4

ORIGINAL ARTICLE

Effects of CT resolution and radiodensity threshold on the CFD evaluation of nasal airflow

Maurizio Quadrio[1] · Carlotta Pipolo[2] · Stefano Corti[1] · Francesco Messina[2] · Chiara Pesci[1] · Alberto M. Saibene[2] · Samuele Zampini[1] · Giovanni Felisati[2]

Received: 14 May 2014 / Accepted: 1 June 2015 / Published online: 10 June 2015

Abstract The article focuses on the robustness of a CFD-based procedure for the quantitative evaluation of the nasal airflow. CFD ability to yield robust results with respect to the unavoidable procedural and modeling inaccuracies must be demonstrated to allow this tool to become part of the clinical practice in this field. The present article specifically addresses the sensitivity of the CFD procedure to the spatial resolution of the available CT scans, as well as to the choice of the segmentation level of the CT images. We found no critical problems concerning these issues; nevertheless, the choice of the segmentation level is potentially delicate if carried out by an untrained operator.

Keywords Nasal cavities · Fluid dynamics · Computer simulation

1 Introduction

The wide incidence of nasal breathing difficulties (NBD) is well assessed [25]; in recent years, functional endoscopic sinus surgery (FESS) became the technique of choice for the treatment of chronic NBD. FESS is minimally invasive and carried out endoscopically; it may involve inferior and/or middle turbinoplasty, and opening of the paranasal sinuses, depending upon anatomy, specific clinical condition and surgeon's judgment. FESS, often coupled with septoplasty, is aimed to re-establish adequate nasal aerial flow, to increase sinus ventilation and to improve sinus drainage [9, 19, 24].

However, assessing the relevance of any given anatomic anomaly (and, consequently, its surgical modification importance) on the overall nasal flow quality is still a daunting task. Patient history and clinical examination are obvious starting points, though subjective to a certain degree. Moreover, septal deviation and other anatomical alterations which commonly occur in the population often do not correspond to functional alterations. Therefore, it is not always possible to establish a causal link between the apparent status of the nose and the disruption of its physiological function. For example, the subjective sensation of good nasal airflow, the so-called nasal patency, has a great importance in patients with NBD, despite often bearing little to no relationship to the actual physical aerodynamic resistance or drag experienced by the airflow in the nose [18, 31]. Furthermore, surgical procedures are typically carried out according to the surgeon's own experience. As a consequence, rationally and reliably predicting the overall effect of any single surgical maneuver on the whole nasal flow is essentially impossible. Even the consequences of a given surgery-induced modification of the inner-nose geometry upon the local airflow quality cannot be fully predicted, the same holds true for the effects of these procedure on humidification, possible crusting, bleeding, etc.

Our limited understanding of the details of the flow field is partly due to the lack of proper diagnostics. In the past, cadaver noses or models reconstructed from CT and MRI images have been used to study the general characteristics of nasal airflow [1]. Such models, however, were inconvenient or inaccurate [10], and their help is limited in view of a patient-specific approach. Acoustic rhinometry is an

✉ Maurizio Quadrio
maurizio.quadrio@polimi.it

[1] Department of Aerospace Science and Technologies, Politecnico Milano, Via La Masa 34, 20156 Milan, Italy

[2] Otorhinolaryngology Unit, Head and Neck Department, San Paolo Hospital, Università degli Studi di Milano, Via di Rudinì 8, 20142 Milan, Italy

effective, noninvasive test [4]. It provides a detailed evaluation of the change of the cross-sectional area of the airways as a function of the distance from the nares. Unfortunately, it cannot evaluate the flow field, but only the shape of its boundaries. Hence, rhinomanometry is the only exam that, with a relative accuracy, can evaluate the nasal aerial patency as a function of overall pressure/flow rate [23]. However, rhinomanometry cannot analyze any detail of the flow (e.g. specifically in the crucial region of the inferior and middle meati) and only provides a global assessment descending from a very complex fluid dynamical pattern.

Recent progresses in modern computational fluid dynamics (CFD) and computer technologies suggest new ways to improve our understanding of nasal airflow. The Navier–Stokes partial differential equations that govern the dynamics of fluids became solvable numerically, most typically within the Reynolds-average framework (RANS), also in complex geometries like those typical of the nasal cavities. In the RANS approach, the governing equations are first averaged in time, so that temporal and small-scale spatial turbulent fluctuations are averaged out, and then numerically solved to obtain the time-mean flow. However, the time-mean effect of the velocity fluctuations upon the mean flow is of paramount importance and must be properly modeled within the RANS approach: This is accomplished through one of the many available so-called turbulence models [20]. Outstanding existing CFD-based works [3, 29, 30] successfully studied the whole respiratory system, focusing on the lower airways and lungs. They often resort to a multi-scale approach to deal with the extremely small spatial scales encountered in the lungs and use rather sophisticated physical models. As far as the upper airways are concerned, the pioneering work by [6] used an extremely simplified computational model to study the flow field within the nasal cavities. Other early CFD attempts to address the trans-nasal aerodynamics using various CT-generated three-dimensional geometries (e.g. [14]) were based on low-fidelity flow models, and did not reach further a qualitative description of the salient global features of the flow. The quality of the numerical prediction has steadily improved over time, until, very recently, CFD has been proposed [2, 22, 28, 34] as a viable tool to support patient-specific pre-surgical planning, leading to the so-called virtual surgery. Several problems, however, are still standing, and the daily use of such tools in the clinical practice remains quite far from reality. For example, [22] pointed out that the operator time required to carry out the entire computational procedure is affordable at research level, but not in everyday clinical practice. A recent review from [21] identifies and critically dissects the main challenges to address for CFD to become clinically useful.

This paper describes a preliminary step toward the long-term goal of making CFD a useful tool for ear, nose and throat (ENT) surgeons. A challenging goal indeed, as validated and highly reliable CFD results are mandatory. For example, one of the most obvious issues to be addressed is the critical choice of the mathematical models employed to represent flow physics in the numerical simulation. The present paper addresses two preliminary, but essential, nevertheless, features of the procedure: (1) How final results are affected by the segmentation threshold used to convert the CT images into a three-dimensional computational volume mesh and (2) How final results are affected by the quality of the CT scan, particularly with regard to the axial gap between consecutive slices. Checking on these prerequisites is helpful in preliminarily assessing the feasibility of a CFD-based procedure that aims at wide clinical deployment. We believe that a procedure requiring an *ad-hoc* imaging has reduced potential to attract large clinical audiences. Hence, in the present paper, we use simple flow models, by considering either a laminar flow in the nasal cavity or a turbulent flow through a standard ($k-\omega-$ SST, [15]) turbulence model. Discussing the criteria to compare various mathematical (turbulence) models, as done for example in [11–13, 32], or evaluating the need to go beyond RANS simulations, is outside the scope of the present paper.

2 Methods

The study was approved by the internal IRB of the San Paolo Hospital, University of Milan. From a pool of about 200 NBD patients who underwent a head CT scan, we selected a 67-year-old male patient who showed a normal sinonasal anatomy. The patient had no septum deviation; his sinuses and nasal conchae were normal; only the inferior nasal conchae showed a mild and symmetrical hypertrophy.

The patient underwent a plain head CT scan with a 64-row multi-detector CT (VCT, General Electric Healthcare, Wisconsin, USA), receiving a 1.9 mSv effective dose. The scanner has a 512×512 matrix, accounting for a $0.49\,\text{mm} \times 0.49\,\text{mm}$ spatial resolution in the sagittal–coronal plane and a 0.625 mm gap between consecutive axial slices. The whole study was composed by 350 native images. For speculative purposes, we asked the radiologists to carry out an additional reconstruction with 1.25 mm axial gap, discarding every second image, thus allowing us to compare different resolution scans without exposing the patient to further doses of radiations.

The images from the CT scan were first manipulated with the open-source software 3D-Slicer [7]. 3D-Slicer is a software platform designed for analysis and visualization of medical images and for research in image-guided therapy; it was adopted as the software of choice also because

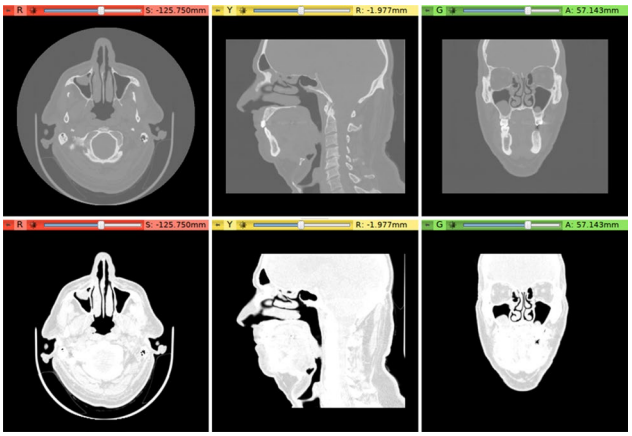

Fig. 1 Example of the raw CT images rendered on a *grayscale lookup table*, with a linear scale (*top*) and with emphasis on air in the CT volume (*bottom*)

Fig. 2 Zoomed-in coronal section: The air-filled spaces shown in *black* correspond to the three meata, the maxillary sinuses and some of the anterior ethmoidal cells. The non-interpolated contour corresponding to the segmentation threshold of HU = 220 separates the reconstructed inner and outer volume, drawn in *green* and is superimposed to the interpolated CT image in *gray*

it is free, open-source and available on multiple operating systems. 3D-Slicer is used to convert the CT images into an accurate geometrical description of the boundary of the volume of interest, through image segmentation and volume reconstruction.

Figure 1 shows the rendering of raw images based on a grayscale lookup table, before (top) and after (bottom) application of a filter to emphasize the boundary of the air-filled volume of interest within the CT volume.

Figure 2 shows a zoomed-in coronal section, where the narrow airway ducts made by the meati, separated by the septum, can be observed. On the sides, maxillary sinuses and ethmoidal structures can also be seen. Figure is based on the original CT image, where pixel intensity is shown in grayscale levels, to which the choice of a segmentation level is applied. The green area thus marks the volume that is considered as not air filled and hence excluded from the simulation; the boundary of the green area shows the native (non-interpolated) resolution of the scan.

After selecting the volume of interest and segmenting the image, the reconstructed three-dimensional geometry is exported and saved into a STereoLithography (STL) file. A small amount of smoothing is applied to the reconstructed surface before exporting to STL, to avoid small-scale irregularities. The default option of 3D-Slicer (10 sinc-based smoothing iterations) is used; this option has been found to be enough to remove pixel-level irregularities while preserving all the significant small-scale features of the anatomy. The smoothing phase, however, can potentially be critical in determining the quality of the final reconstructed volume. The adequacy of the level of smoothing is not discussed in this study and will be addressed in future.

So far, we have described the part of the procedure where the DICOM database is read into 3D-Slicer, a segmentation level is chosen, its suitability verified and the three-dimensional reconstruction of volumes is carried out and written into a STL file after proper smoothing. Overall, these steps predate the creation of the actual computational mesh where the differential equations of motion are discretized and solved. This typically requires 15–30 min of operator time, as the only non-trivial step is the choice of the segmentation level. Time required for this step will depend on the experience of the operator and the quality of CT scans.

The reconstructed geometry is then used as an input for the subsequent analysis, first by generating the computational mesh to be used by the CFD software. We use the open-source CFD package OpenFOAM, which is based upon the work of Weller et al. [27]. OpenFOAM is a general C++ library, based on finite volume discretization, which allows building solvers for partial differential equations. The package contains a tool, called `snappyHexMesh`, that converts the STL geometry into a computational mesh. It first fills with hexahedrals (castellated mesh) the whole volume of interest, delimited by the reconstructed boundary; the castellated mesh is then deformed to snap onto the actual boundary; additional layers of cells are ultimately added near the solid boundaries of the volume of interest. This is intended to allow better coping with the flow boundary layers which develop along the geometric boundaries where the flow velocity obeys the no-slip condition.

The last phase is the actual execution of the flow solver, which computes flow variables like velocity, vorticity and pressure fields. The OpenFOAM package contains a number of specialized and pre-made flow solvers. In the present

work, we employ the standard `pimpleFoam` solver for the incompressible Reynolds-averaged Navies–Stokes equations, with either laminar flow or a turbulence model adopted for their closure. The fluid is air at ambient temperature, with kinematic viscosity $\nu = 1.5 \times 10^{-5}\,\mathrm{m}^2/\mathrm{s}$. The employed solver is based on a mixed PISO-SIMPLE strategy [8] for pressure–velocity coupling and is used with second-order discretization schemes for every differential operator of the PDEs. As heat and mass transfer phenomena are not considered, the Reynolds-averaged equations of motions express conservation of mass and momentum in the incompressible case, and read:

$$\nabla \cdot \overline{\mathbf{u}} = 0 \tag{1}$$

$$\frac{\partial \overline{\mathbf{u}}}{\partial t} + \nabla \cdot \left(\overline{\mathbf{u}}\,\overline{\mathbf{u}} + \overline{\mathbf{u}'\mathbf{u}'}\right) + \frac{1}{\rho}\nabla \overline{p} = \nu \nabla^2 \overline{\mathbf{u}} \tag{2}$$

where $\overline{\mathbf{u}}$ is the velocity vector averaged in time (on a time scale shorter that a typical flow timescale), $\mathbf{u}'$ its fluctuations around that mean and $\overline{p}$ the mean pressure. The term $\overline{\mathbf{u}'\mathbf{u}'}$ is not known as a function of the mean velocity field $\overline{\mathbf{u}}$, as it represents the whole effect of turbulence upon the mean flow, and needs some modeling assumptions for the above equations to be solvable.

Boundary conditions for the differential system (1)–(2) need to be specified. The reconstructed surface of the nasal passageways is considered as a solid wall, where no-slip and no-penetration boundary conditions are applied, i.e., $\overline{\mathbf{u}} = 0$. The two extremes of the actual volume of interest for nasal aerodynamics are the nostrils, representing the inlet side of the boundary for an inspiration, and the region of the glottis at the outlet boundary. In many of the existing studies, velocity is considered as known and enforced with a Dirichlet-type boundary condition at the inflow; a zero-gradient condition is selected for the velocity vector at the outflow. Since the boundary condition enforced at the inflow turns out to be potentially critical in determining the quality of the final solution, given its proximity to the very important area of the nasal valve, following [5] we also compute the flow field in an additional region made by a box, with dimensions $240 \times 300 \times 200\,\mathrm{mm}$ that surrounds the whole head of the patient. The flow is thus driven by an assigned pressure difference $\Delta\overline{p}$ between the outer surface of the box and the region of the throat. A zero-gradient condition at the inflow is enforced on the velocity components at the faces of the box, thus allowing the full velocity field at the nostrils to be reliably computed as part of the solution process instead of being arbitrarily assigned as a boundary condition.

Figure 3 shows the size of the outer box relative to the patient's head and the nasal passageways that represent the volume of primary interest. Figure 4 shows a view of the computational domain contained between the outer box and the patient's head. The volumetric computational grid is plotted onto the surface and different grid densities can be appreciated in correspondence to face areas where the internal volumes belong to the nasal cavities, where most of the computational effort will be spent. The inner grid is further layered to better resolve the steep velocity gradients taking place in the proximity of the solid boundaries. Notice that the extent of the external box has not been determined through an optimization process and should be rather considered as a conservative initial choice. In particular, the posterior volume is likely to be unnecessary; optimization of the outer volume and its cell size is ongoing work.

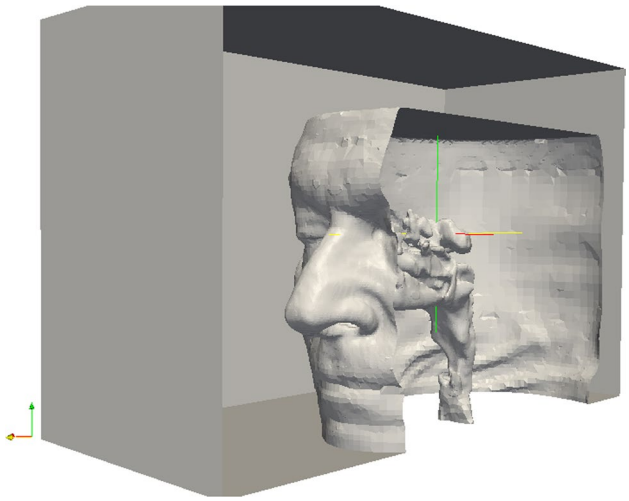

Fig. 3 Three-dimensional view of the surface described by the STL file after the segmentation process. The nasal passageways and the large volume occupied by the nasal sinuses are evident, as well as the patient's face

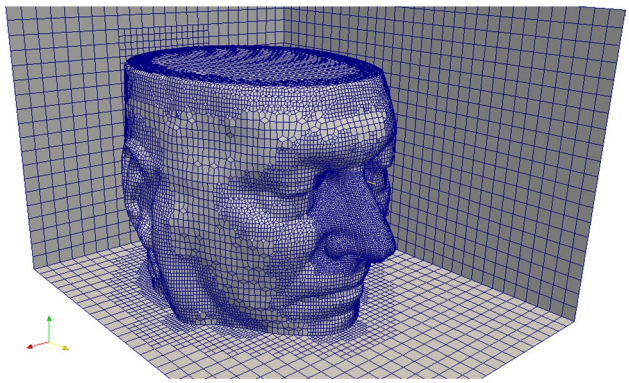

Fig. 4 Three-dimensional view of the computational domain (external part). The gridded volume is the whole air-filled volume, i.e., the portion surrounding the patient's head and delimited by the outer cube, plus the volume occupied by the nasal passageways down to the nasopharynx and throat. The surface-plotted grid gives a feeling of the spatial resolution employed in the internal volumes

2.1 Details of the simulations

The simulations described below concern a steady inspiration forced by a pressure difference of $\Delta\overline{p} = 130\,\text{Pa}$ between the outer ambient and the larynx, as done in [32]. This pressure difference corresponds to a mild-to-intense exercise [26]. Although the boundary conditions are stationary, a transient solver is used to compute up to 0.75 s of inspiration starting from an initial condition where the internal velocity and pressure field are zero and the initial transient decays quite rapidly. The time step is 3×10^{-6} s.

As previously stated, it is not our aim here to discuss the choice of the best mathematical and closure model for the flow, Therefore, we rely on the current consensus [16, 17] concerning this kind of simulations, i.e., when a turbulence model is required, the $k-\omega-$ SST RANS model is the best and nears the quality expected by the higher-fidelity LES. The following results are presented for a laminar simulation, i.e., one where the Navier–Stokes equations are solved without a turbulence model, and for a turbulent simulation where the Bousinnesq hypothesis of turbulent eddy viscosity ν_t is adopted and the $k-\omega-$ SST turbulence model [15] is employed. The $k-\omega-$ SST model solves additional PDEs for the turbulent kinetic energy k, and an additional, scale-setting turbulence variable ω that represents a specific dissipation rate of k. In its simplest form, the turbulent viscosity ν_t is given by $\nu_t = k/\omega$. Wall functions are used to avoid massive clustering of grid points near the walls.

A grid refinement study has been carried out, evaluating results obtained with meshes containing from 0.3 to 5 millions cells for both the laminar and the turbulent case. Although the less detailed mesh presented rather evident geometrical differences (e.g. the unrealistic representations of the volumes of the large sinuses), the global features of the flow field were always well predicted. As the two largest meshes (with 2.4 and 5 millions cells) yielded a flow rate that was unchanged within <0.1 %, the remaining part of the computational study was carried out on the mesh with 2.4 millions cells.

In terms of computing time, the present simulations are rather small, with most of the cases having a mesh composed by 2.4 millions cells. We thus limit parallel computing to 4 cores for each case, which yields a linear speedup. Computing 0.75 s of steady inspiration requires about 4 days of wall clock time by using Intel Xeon CPUs at 3.16 GHz. Thanks to the number of processors available, the same time is sufficient to carry out the whole parametric study by running all the required cases in parallel. The computational cost of the turbulent simulation, owing to the additional differential equations, is about twice that of the laminar simulation. Depending upon the particular flow model adopted, the computational requirements are greatly varying. For example, a steady-state simulation would require far less computational resources, amounting to 2 h on a laptop for the laminar case. A comparable wall clock time could be achieved for a time-dependent case, if required, by exploiting a larger number of CPUs.

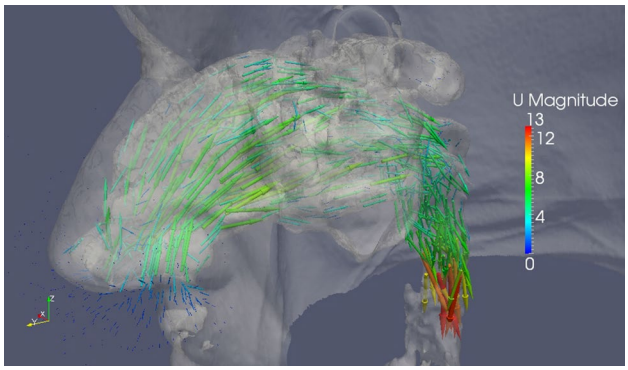

Fig. 5 Three-dimensional view of the nasal cavity flow, corresponding to a steady inspiration. *Arrows* show the local velocity vector, with *size* and *color* determined from its modulus, measured in m/s

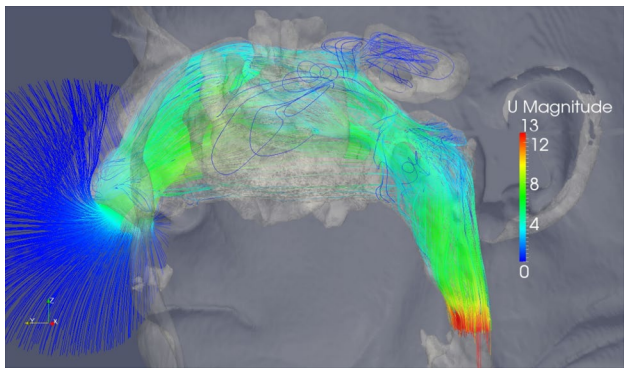

Fig. 6 Three-dimensional view of the nasal cavity flow, corresponding to a steady inspiration. Flow is depicted here through the trajectory of massless lagrangian tracers, released in the region in front of the patient's head and *color-coded* with the local velocity, measured in m/s

3 Results

First, an overall assessment of the results, corresponding to the flow field obtained with the laminar model, is provided. Figure 5 shows a three-dimensional, qualitative view of the computed solution, visualized in terms of its velocity field. The spatial rate of change of the velocity in the area of the turbinates can be appreciated thanks to the color and size of the arrows, which is proportional to the magnitude of the velocity vector. Figure highlights the high velocity values reached in the downstream portion of the domain, due to the gradually restricted cross section. Similarly, Fig. 6 shows the presence of a recirculating region in

correspondence of the maxillary sinus, and—more importantly—on the uppermost region of the nasal cavity, at the upper boundary of the so-called olfactory cleft where most of the olfactory receptors are located. Lastly, Fig. 7 emphasizes how the local shape of the nasal passageways induces strong longitudinal variations of the flow when passing from the nasal vestibulum to the nasopharynx. It can be visually appreciated how the middle meatus and, to a lower extent, the inferior meatus play a major role and account for most of the flow rate, as already known from several previous studies, e.g. [12].

A radiodensity threshold value must be chosen to identify the geometric boundary of the volume of interest for the CFD analysis, in order to initiate the construction of a three-dimensional model by using edge detection image processing algorithms. Radiodensity is typically expressed in the Hounsfield unit (HU) scale, in which the radiodensity of distilled water at standard pressure and temperature is defined as 0 HU, while the radiodensity of air is defined as 1000 HU. Thus, a change of one Hounsfield unit represents a change of 0.1 % of the attenuation coefficient (AC) of water, since the AC of air is nearly zero. For reference, fat AC is around 100 HU, muscles AC are 40 HU, and bones AC start from 300 HU onward.

To assess the importance of the radiodensity threshold, we have carried out a series of CFD simulations (on a nominally identical mesh) where the threshold is systematically varied. In this section, we only consider laminar simulations. With the flow being always driven by the same pressure difference between the outer ambient and the throat, measuring the flow rate through the nostrils gives an indication of the global sensitivity of the CFD results to the segmentation threshold. Figure 8 plots the values, expressed in liters per second, of the observed flow rate in selected regions of the flow field, as a function of the segmentation threshold expressed in HU. The threshold is varied around the empirically determined best value of 230 HU. Two extreme cases, with the threshold set very low at 120 HU and very high at 280 HU, are also considered. These extreme cases are way beyond what an experienced user could select, as exemplified in Fig. 9 where too low a threshold is shown to remove large portions of the reconstructed volume. This is due to the change in connectivity, as too low a threshold does not correctly represent the small *ostii* connecting the main airways to the large volumes of the sinuses. It must be said that the dimensions of the *ostii* significantly vary across various subjects. However, especially for those connecting the airways to the largest sinuses, their typical size is large enough compared to the CT resolution that changing the HU threshold within reasonable limits only modifies their detailed contour and does not affect the global topology.

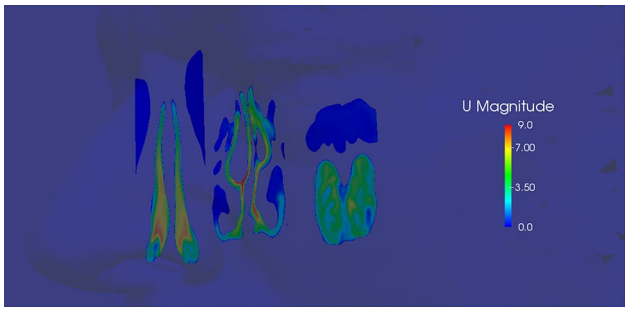

Fig. 7 *Colored contours* for the modulus, measured in m/s, of the velocity vector in three coronal sections taken at different positions

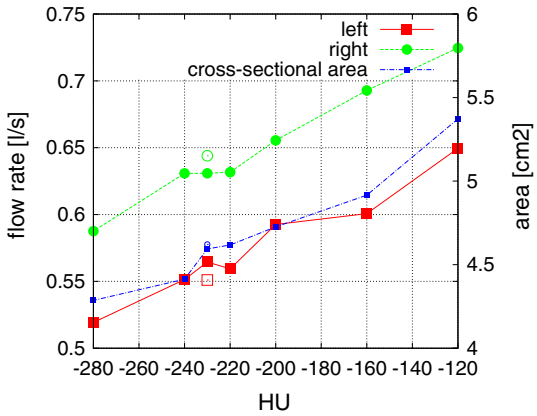

Fig. 8 Flow rate (expressed in liters per second) through the *right* (*green curve*, *circles*) and *left* (*red curve*, *squares*) nostrils, as a function of the radiodensity threshold (expressed in HU) employed for the reconstruction of the three-dimensional volume of interest. The plateau between 240 and 220 HU can be appreciated. The open symbols are for the low-quality reconstruction at 230 HU (see *text*). The *blue dashed line* with *small squares* shows the variation of the cross-sectional area of the intermediate coronal section shown in Fig. 7

Figure 8 in particular quantifies how the flow rate changes with the chosen threshold. The flow rate is evaluated in a separate manner for the left and right nostril. The nearly monotonic behavior of the data implies that the reconstructed volume consistently increases when the threshold is increased: as the flow is driven by a fixed pressure difference, a larger volume, with a larger cross section, implies a larger flow rate. This is made evident by the dashed line, that plots the cross-sectional area of the middle coronal section of the nasal airways already shown in Fig. 7: Although there is no reason to expect a precise one-to-one correspondence between the cross-sectional area at that particular location and the flow rate, which is a global quantity, it is clear that most of the variations are explained by the lower nasal resistance offered by wider airways.

A visual inspection of the impact of changing the HU threshold on the flow field is given in Fig. 10 that shows

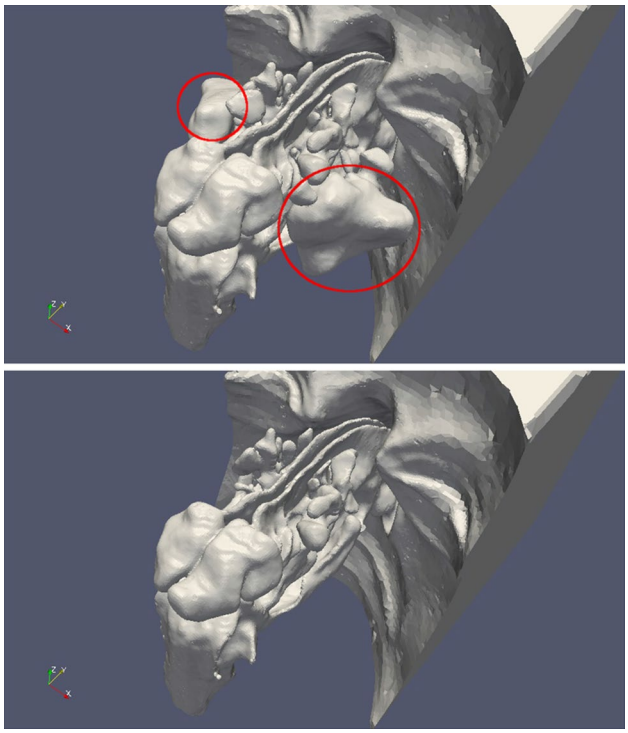

Fig. 9 Effect of the radiodensity threshold on the reconstructed geometry. By going from 200 HU (*top*) to 280 HU (*bottom*), the internal volume becomes progressively reduced, and several portions of the volume related to large sinuses (*highlighted* in the *top figure* with *red circles*) are excluded

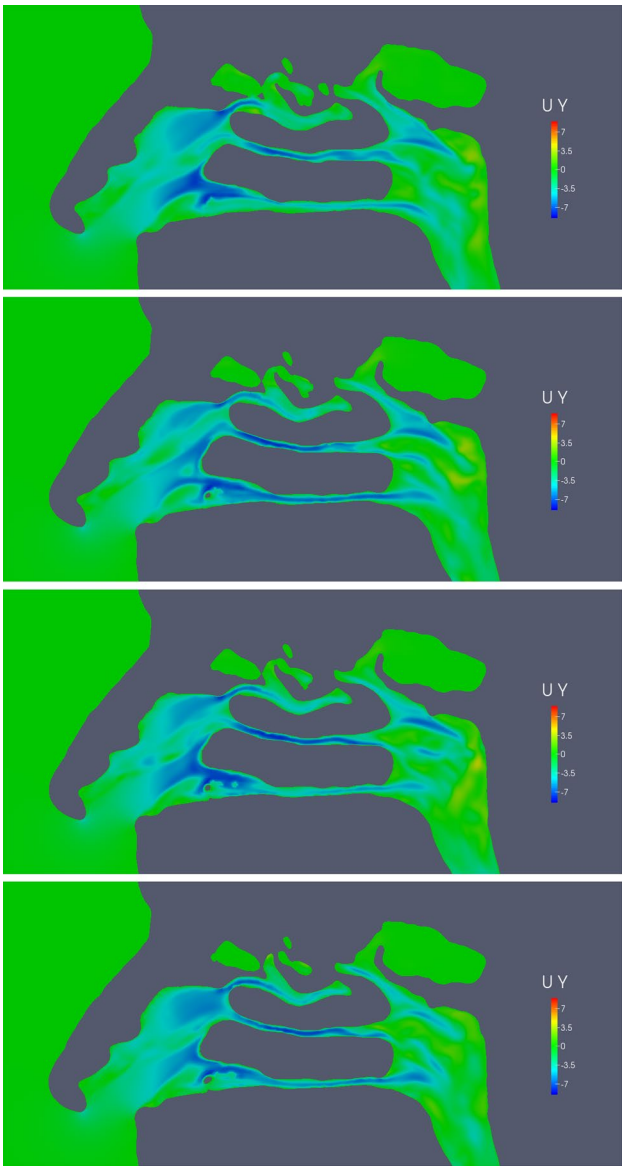

Fig. 10 Effect of the radiodensity threshold on the computed posterior–anterior velocity field, measured in m/s, as seen in a sagittal section passing through the right nasal passageway. From *top* to *bottom*: threshold at 120, 220, 230, 280 HU. Positive velocity is from *right* to *left*

a color map for the posterior–anterior velocity component (positive from right to left). Small changes in the reconstructed anatomy and in the connectivity to the ethmoidal cells can be appreciated; however, no significant changes are observed in terms of the velocity field, in line with the above observation that the changes in the flow rate can be mostly ascribed to changes in cross-sectional area.

The CT scan we employed has an axial gap of 0.625 mm between consecutive axial slices. We had the same scan reconstructed at a larger axial gap of 1.25 mm, so that the results for an otherwise identical procedure can be meaningfully compared. In Fig. 8, the lower-quality mesh reconstructed for 230 HU is denoted with open symbols. Little changes can be noticed.

4 Discussion

We have described a numerical procedure for a CFD study of the flow in the nasal airways for a patient-specific anatomy. The preliminary step of building the computational mesh, which is essential in determining the quality of the final results, is designed once and for all and results in an extremely convenient sequence of operations. The computational domain has been chosen to entirely surround the patient's head. Although this is subject to further optimization (a crude estimate of the computational overhead related to solving the fluid equations in the outer region is a significant 40 % of the overall computational cost), we consider this a fair price to be paid for getting rid of the arbitrary assignment of fictitious boundary conditions upon a very sensitive region of the flow field (the nostrils). This aspect is bound to become even more important when the expiration phase of the respiratory cycle is considered. Figures 5 and 6 highlight how a non-trivial velocity field

develops near the nose tip: this would be difficult to be accounted for correctly, should the inlet boundary conditions be imposed straight at the nostrils. Moreover, the flow velocity outside the nasal cavity is negligibly small everywhere but in the immediate vicinities of the nostrils, lending support to the simple zero-gradient boundary condition employed on the outer surface of the computational box. In terms of operator time, the only time-consuming part of the procedure is the segmentation of the CT image leading to the STL geometry, which requires 15–30 min. We regard this as a very positive result, since only a few years ago reducing such time down to a few days was described as an important advancement [33].

The availability of the full velocity field allows the identification of its main features and a thorough examination of their functional significance. For example, from Fig. 6, the sophisticated fluid dynamical design of the nasal cavities can be appreciated: Generally disadvantageous recirculation regions are present only where a longer residence time becomes advantageous for the odorant molecules to impress the olfactory receptors more effectively. However, owing to the lack of true in vivo validation, such results should always be critically considered. For example, even though several available CFD results are computed with turbulence models, depending upon the flow rate, the nasal flow can be hardly turbulent in most of the volume, although it is clearly massively separated (in the available literature, the different notions of turbulent flow and of unsteady separated flow are sometimes confused). The specific flow model did not produce a significant effect on the global value of the flow rate, which is found to differ by $< 1\ \%$ between the laminar and turbulent simulations, further indicating that in the present case the majority of the flow develops in the laminar regime.

In this paper, we have particularly focused on the effect of the choice of the segmentation threshold, something that has not received much attention in the literature. Indeed, significantly changing the value of the threshold introduces evident visual effects in the reconstructed volume. In general, decreasing the threshold value implies that the air volume within the nasal cavity decreases; at some point, the large sinuses, which communicate with the main ducts through relatively small orifices, the *ostii*, become excluded from the volume of interest, as shown in Fig. 9.

In terms of quantitative results, the parametric study presented here explicitly addresses for the first time the sensitivity of the solution (or, at least, of some global characteristics of the solution) to the segmentation threshold. It is interesting to note that our results (cfr. Fig. 8) suggest, for both nostrils, the existence of a plateau between 240 and 220 HU where the flow rate presents minimal changes. This is precisely where visual inspection indicates the geometric reconstruction to be most accurate. Moreover, it can be appreciated how only the extreme values of threshold produce reconstructed volumes with significant differences. However, even in these cases, the flow field does not show evident misrepresentations and the computed global quantities present only modest variations, owing to the limited impact of the large sinuses on the overall flow features. Most of the changes in a global quantity like the flow rate can be simply ascribed to the change in volume, with the inner velocity field being only marginally affected by the geometric changes.

The comparison of the flow rates in the right and left passageways shows that halving the axial resolution of the CT scan affects a global result like the flow rate by a change of the order of $1\ \%$. This can be appreciated by looking again at Fig. 8, where the points from the lower-resolution reconstruction are indicated with open symbols. Overall, these changes are entirely in line with the small changes that are introduced by the unavoidable uncertainty in the segmentation levels. However, there is an indication that, owing to the complex three-dimensional geometry of the nasal cavity, it would be desirable to employ a CT scan with as isotropic a spatial resolution as possible.

5 Conclusions

In this work, we have described a preliminary, yet essential step toward making CFD analysis of the nasal passageways a useful tool in the daily ENT practice. Two issues are discussed: How the quantitative outcome of the CFD analysis depends upon the quality of the available CT scan, and how the choice for a radiodensity threshold affects the accuracy of the reconstructed nasal cavity and, consequently, the computed flow field. Our results indicate that a standard CT scan should be enough to produce robust results. On the other hand, the choice of the radiodensity threshold may become a critical issue, since global features of the flow like the mass flow rate show a non-negligible dependence upon this parameter. However, most of this dependence can simply be ascribed to the volumetric changes of the considered geometry, with the inner flow field being only marginally affected. Moreover, we have found that, when the threshold is set by the operator in such a way that the reconstruction presents reasonable details from an anatomical standpoint, a plateau does exist where even the global flow rate depends weakly, if at all, on the segmentation threshold.

Of course, it remains to be assessed whether and how this relative robustness of the CFD procedure applies to the fine-scale details of the flow. This is a necessary further step that can be meaningfully carried out once a particular mathematical and physical model (e.g. Large Eddy Simulation vs Reynolds-Averaged Navier–Stokes equations) and

a specific turbulence model are chosen. Thus, the results obtained so far are not yet conclusive in this respect, but do allow for an optimistic outlook.

Acknowledgments Part of the calculations presented here has been carried out on the Lagrange supercomputer of the CINECA (formerly CILEA) computing center in Milano/Bologna, Italy. We thankfully acknowledge their support.

References

1. Arbour P, Bilgen E, Girardin M (1985) Experimental study of nasal velocity fields in a human nasal fossa by laser anemometry. Rhinology 23:201–207
2. Chen X, Lee H, Chong V, Wang D (2009) Assessment of septal deviation effects on nasal air flow: a computational fluid dynamics model. Am Laryngol Rhinol Otol Soc 119:1730–1736
3. Choi J, Tawhai MH, Hoffman EA, Lin C-L (2009) On intra- and inter-subject variabilities of airflow in the human lungs. Phys Fluids 21:101901
4. Clements PA, Gortds F (2005) Standardisation Committee on Objective Assessment of the Nasal Airway, IRS, and ERS Consensus report on acoustic rhinometry and rhinomanometry. Rhynology 43(3):169–179
5. Doorly D, Taylor D, Gambaruto A, Schroter R, Tolley N (2008) Nasal architecture: form and flow. Philos Trans R Soc 366:3225–3246
6. Elad D, Liebenthal R, Wenig B, Einag S (1993) Analysis of air flow pattern in the human nose. Med Bio Eng Comput 31:585–592
7. Fedorov A, Beichel R, Kalpathy-Cramer J, Finet J, Fillion-Robin JC, Pujol S, Bauer C, Jennings D, Fennessy F, Sonka M, Buatti J, Aylward S, Miller J, Pieper S, Kikinis R (2012) 3D slicer as an image computing platform for the quantitative imaging network. Magnetic Resonance Imaging p. 22770690. http://www.arxiv.org
8. Ferziger JH, Peric M (2013) Computational Methods for Fluid Dynamics. Springer, Berlin
9. Frank DO, Zanation AM, Dhandha VH, McKinney KA, Fleischman GM, Ebert CS Jr, Senior BA, Kimbell JS (2013) Quantification of airflow into the maxillary sinuses before and after functional endoscopic sinus surgery. Int Forum Allergy Rhinol. 10:834–40
10. Hahn I, Scherer P, Mozell M (1993) Velocity profiles measured for airflow through a large-scale model of the human nasal cavity. J Appl Physiol 75:2273–2287
11. Hörschler I, Schröder W, Meinke M (2010) On the assumption of steadiness of nasal cavity flow. Biomechanics 43:1081–1085
12. Kleinstreuer C, Zhang Z (2010) Airflow and particle transport in the human respiratory system. Ann Rev Fluid Mech 42:301–334
13. Leong S, Chen X, Lee H, Wang D (2010) A review of the implications of computational fluid dynamic studies on nasal airflow and physiology. J Rhinol 48:139–145
14. Martonen T, Quan L, Zhang Z, Musante C (2002) Flow simulation in the human upper respiratory tract. Cell Biochem Biophys 37:2736
15. Menter F (1994) Two-equation eddy-viscosity turbulence models for engineering applications. AIAA J 32(8):1598–1605
16. Mihaescu M, Mylavarapu G, Gutmark EJ, Powell NB (2011) Large Eddy simulation of the pharyngeal airflow associated with Obstructive Sleep Apnea Syndrome at pre and post-surgical treatment. J Biomech 44(12):2221–2228
17. Mylavarapu G, Murugappan S, Mihaescu M, Kalra M, Khosla S, Gutmark E (2009) Validation of computational fluid dynamics methodology used for human upper airway flow simulations. J Biomech 42(10):1553–1559
18. Nathan A, Eccles R, Howarth P, Steinsvag S, Togias A (2005) Objective monitoring of nasal patency and nasal physiology in rhinitis. J Allergy Clin Immunol 115(3):S442–S459
19. Pötker DM, Smith TL (2007) Adult chronic rhinosinusitis: surgical outcomes and the role of endoscopic sinus surgery. Curr Opin Otolaryngol Head Neck Surg 15(1):6–9
20. Pope S (2000) Turbulent flows. Cambridge University Press, Cambridge
21. Quadrio M, Pipolo C, Corti S, Lenzi R, Messina F, Pesci C, Felisati G (2013) Review of computational fluid dynamics in the assessment of nasal air flow and analysis of its limitations. Eur Arch Otorhinolaryngol. doi:10.1007/s00405-013-2742-3
22. Rhee J, Pawar S, Garcia G, Kimbell J (2011) Toward personalized nasal surgery using computational fluid dynamics. Arch Facial Plast Surg E1–E6
23. Schumacher M (2004) Nasal dyspnea: the place of rhinomanometry in its objective assessment. Am J Rhinol 18(1):41–46
24. Shivakumar T, Sambandan AP (2011) Retrospective analysis of the effectiveness of functional endoscopic sinus surgery in the treatment of adult chronic rhinisinusitis refractory to medical treatment. Indian J Otolaryngol Head Neck Surg 63(4):321–324
25. Stewart M, Ferguson B, Fromer L (2010) Epidemiology and burden of nasal congestion. Int J Gen Med 3:37–45
26. Wang D, Lee H, Gordon R (2012) Impacts of fluid dynamics simulation in study of nasal airflow physiology and pathophysiology in realistic human three-dimensional nose models. Clin Exp Otorhinolaryngol 5(4):181–187
27. Weller H, Tabor G, Jasak H, Fureby C (1998) A tensorial approach to computational continuum mechanics using object-oriented techniques. Comput Phys 12:620–631
28. Xiong G, Zhan J, Zuo K, Li J, Rong L, Xu G (2008) Numerical flow simulation in the post-endoscopic sinus surgery nasal cavity. Med Bio Eng Comput 46:1161–1167
29. Yin Y, Choi J, Hoffman EA, Tawhai MH, Lin C-L (2010) Simulation of pulmonary air flow with a subject-specific boundary condition. J Biomech 43(11):2159–2163
30. Yin Y, Choi J, Hoffman EA, Tawhai MH, Lin C-L (2013) A multi- scale MDCT image-based breathing lung model with time-varying regional ventilation. J Comput Phys 244:168–192
31. Zhao K, Blacker K, Luo Y, Bryant B, Jiang J (2011) Perceiving nasal patency through mucosal cooling rather than air temperature or nasal resistance. PLoS One 6(10):e24,618
32. Zhao K, Dalton P, Yang G, Scherer P (2006) Numerical modeling of turbulent and laminar airflow and odorant transport during sniffing in the human and rat nose. Chem Senses 31:107–118
33. Zhao K, Scherer P, Hajiloo S, Dalton P (2004) Effect of anatomy on human nasal air flow and odorant transport patterns: implications for olfaction. Chem Senses 29:365–379
34. Zhu J, Lim K, Thong K, Wang D, Lee H (2014) Assessment of airflow ventilation in human nasal cavity and maxillary sinus before and after targeted sinonasal surgery: a numerical case study. Respir Physiol Neurobiol 194:29–36